

AXISYMMETRIC PLUMES IN VISCOUS FLUIDS

EMMA J. ALLWRIGHT^{1,2}, L. K. FORBES^{✉2} and S. J. WALTERS²

(Received 21 November, 2018; accepted 10 April, 2019; first published online 17 May 2019)

Abstract

We consider fluid in a channel of finite height. There is a circular hole in the channel bottom, through which fluid of a lower density is injected and rises to form a plume. Viscous boundary layers close to the top and bottom of the channel are assumed to be so thin that the viscous fluid effectively slips along each of these boundaries. The problem is solved using a novel spectral method, in which Hankel transforms are first used to create a steady-state axisymmetric (inviscid) background flow that exactly satisfies the boundary conditions. A viscous correction is then added, so as to satisfy the time-dependent Boussinesq Navier–Stokes equations within the fluid, leaving the boundary conditions intact. Results are presented for the “lazy” plume, in which the fluid rises due only to its own buoyancy, and we study in detail its evolution with time to form an overturning structure. Some results for momentum-driven plumes are also presented, and the effect of the upper wall of the channel on the evolution of the axisymmetric plume is discussed.

2010 Mathematics subject classification: primary 76E20; secondary 76E17, 76M22.

Keywords and phrases: Boussinesq fluid, overturning plume, unsteady flow.

1. Introduction

Plumes are ubiquitous in nature, over length scales ranging from the microscopic to the galactic. They may occur when a fluid is injected into an ambient fluid of some different density, or when a light fluid rises through a heavier fluid due to the effects of buoyancy. Perhaps the most enduring images of plumes are those due to volcanic ash clouds or explosions [36]. Other, more exotic, examples also occur, such as the “black smokers” deep within the ocean, where super-heated water may rise from submarine volcanic vents on the sea floor. Remarkably, these vents may even sustain their own populations of thermophilic life forms [27]. Outflows from stars or galaxies sometimes form plumes as they enter the more dense interstellar medium, and these occur over vast length scales and on times spanning millions of years [31]. Similarly, fountains,

¹Mathematics Department, T. U. München, Germany; e-mail: Emma.Allwright@tum.de.

²Department of Mathematics and Physics, University of Tasmania, PO Box 37, Hobart, 7001, Tasmania, Australia; e-mail: Larry.Forbes@utas.edu.au, stephen.walters@utas.edu.au.

© Australian Mathematical Society 2019

which may be thought of simply as plumes of negative buoyancy, occur frequently in nature or are intentionally manufactured, and are discussed in the review by Hunt and Burridge [18]. Hunt and Kaye [19] classified plumes into three broad groups, “lazy”, “pure” or “forced”, based on the value of a particular source parameter. Their focus, however, was strongly on turbulent flow. Turbulent entrainment in plumes has also been addressed more recently by Craske and van Reeuwijk [8].

The study of plumes is closely related to the Rayleigh–Taylor instability, in which a heavier fluid lies above a light fluid, with a sharp interface separating the two. In the classical problem of this type, studied by Lord Rayleigh [28] and Sir G. I. Taylor [32], the two fluid layers were horizontal, so that the undisturbed interface is a flat plane. When a small periodic perturbation is made to this interface, the configuration becomes unstable and, in linearized (small-amplitude) theory, the amplitude of the periodic perturbation grows exponentially with time, with a growth rate determined by the ratio of the densities of the upper and lower fluids. However, as discussed by Sharp [30] and Andrews and Dalziel [2], an exponentially growing amplitude soon violates the linearized assumption of small amplitude size, so that, after some finite time, the predictions of linearized theory no longer apply. Thereafter, nonlinear effects dominate the shape and behaviour of the interface.

Nonlinearity is largely responsible for the overturning profiles of many plumes, since this occurs once the plume has undergone large-amplitude deformation, well outside the domain of validity of linearized analysis. In addition, nonlinear effects are also manifest in other surprising and unexpected ways. When viscosity is ignored, the resulting nonlinear inviscid theory predicts disturbances that grow rapidly, but then numerical methods fail abruptly at a finite time, for reasons that are at first not at all obvious. This is alluded to in the article by Sharp [30]. It turns out that there is a finite critical time at which the *curvature* of the interface becomes infinite, so that the purely inviscid model ceases to be valid after this time. This interfacial singularity was first reported by Moore [25], who used asymptotic methods to estimate the critical time at which it occurs. This time is dependent upon the initial disturbance amplitude and the density ratio of the two fluids. Moore’s work [25] was originally carried out for a related flow (the Kelvin–Helmholtz instability), but a similar situation applies for Rayleigh–Taylor flows [4].

The Moore curvature singularity that forms in inviscid Rayleigh–Taylor flow is a consequence of the fact that the interface is assumed to be an infinitesimally thin vortex sheet. It can, in principle, be avoided if the sharp interface is instead replaced by an interfacial zone of finite width, across which the density changes rapidly but smoothly. This is essentially the approach taken with the “vortex-blob method” pioneered by Krasny [20], which allows the solution to continue beyond Moore’s critical time, even in an inviscid fluid model. Krasny [20] was able to compute numerical solutions for Kelvin–Helmholtz flow, in which the initially sinusoidal disturbance rolled up to form the famous “cat’s eyes” spirals that occur in that flow. Vortex-blob methods have since been critiqued in detail by Baker and Pham [5] in their application to interfacial fluid mechanical problems. When viscosity is re-introduced to these models, this provides

a mechanism by which vorticity may now be generated internally in the fluid, and Forbes [10] showed numerically that small patches of intense vorticity are produced at the precise locations and times at which the Moore curvature singularity would have been generated in a purely inviscid model. These small vorticity patches are then responsible for the overturning of the interfacial zone to form mushroom-shaped plumes at later times.

In astrophysical situations, in particular, Rayleigh–Taylor-type instabilities can occur in geometries other than the purely planar case originally studied by Rayleigh [28] and Taylor [32]. If a light fluid occupies an initially cylindrical region, surrounded by heavier interstellar medium, the interface between them may become unstable if it is disturbed by a shock. This is the Richtmyer–Meshkov instability and has been studied by Matsuoka and Nishihara [23]. They showed that, if the cylinder is initially subjected to a third-mode disturbance, it can develop three plumes surrounding the cylinder and moving outwards with time. A similar result was obtained by Forbes [11] for a Rayleigh–Taylor-type outflow from an initially cylindrical region of light fluid surrounding a line source down the central axis of the cylinder. This source was also massive and so created its own radially symmetrical gravitational field directed inwardly towards the axis of the cylinder. Forbes [11] showed that this cylindrical Rayleigh–Taylor flow also formed curvature singularities at the interface, in an inviscid model of the fluids, but, when viscosity was included, and significantly with a diffuse interfacial zone, then no such singularity could occur. He presented results, qualitatively similar to those of Matsuoka and Nishihara [23], which contained overturning plumes of outflowing light fluid arranged symmetrically around the initial cylinder.

Rayleigh–Taylor-type outflows are also possible in initially spherical geometry and this was investigated by Forbes [12] in an idealized problem in which a central massive young star, modelled as a point source of light fluid, is initially surrounded by a spherical jacket of this lighter fluid, but is embedded in a heavier ambient fluid. A gravitational field is again present, directed centrally inwards towards the star. Here, however, the situation is very different to the cylindrical case. Linearized theory predicts that an initial disturbance to the interface is now most unstable to the *lowest* of the spherical modes, so that a one-sided jet would be expected to form. This is a surprising result, but it turns out to be consistent with a stability equation derived earlier by Mikaelian [24]. Numerical solutions confirmed this prediction and may perhaps even explain the one-sided astronomical outflow studied by Gómez et al. [14] or the one-sided jets computed from a computational fluid dynamics (CFD) code by Lovelace et al. [22].

On a smaller scale, plumes may also occur beneath the ocean, or in volcanic outflows or even in certain manufactured devices. A celebrated model of plumes under such circumstances is the MTT model, named after its inventors Morton, Taylor and Turner [26]. That paper allowed for turbulent behaviour in a plume using an entrainment hypothesis in which there was a horizontal velocity component near the plume, which was assumed to be proportional to the vertical speed within the

plume. The constant of proportionality between the two could then be regarded as an “entrainment coefficient”. More recently, this idea was applied by Letchford et al. [21] to examine transient waves on the surface of a vertical cylindrical plume between two horizontal plates. In that paper, Letchford et al. [21] did not address the question of how such a plume became established, but rather considered that some vertical structure between the two plates was already in existence, so that waves could form on its interface. To address the issue of the initiation of a plume, Russell et al. [29] have recently considered the way in which, in a two-dimensional model, a line source present in the bottom of a channel creates a growing mass of lighter-density fluid that moves vertically, before forming an overturning mushroom-shaped plume and then mixing laterally in the channel. Previously, Hocking and Forbes [16] had studied the steady inviscid behaviour of a two-dimensional plume in a channel, and obtained results in which the lighter fluid, introduced through a vent at the bottom of the channel, could rise up and flow outwards along the ceiling; to some extent, the work of Russell et al. [29] shows how viscosity may alter that result.

The present paper seeks to extend the analysis of Russell et al. [29] to three-dimensional geometry, albeit under the assumption that circular symmetry about a vertical axis is maintained throughout the plume’s development. Originally, we aimed to consider a point source embedded in the bottom of a channel, corresponding to the line source in the two-dimensional theory of Russell et al. [29]. However, this posed difficulties, both analytical and numerical, in obtaining a convergent expression for certain flow variables in the irrotational background flow, and a nonsingular inlet flow was found to be required. Accordingly, here we instead allow the introduction of the less-dense fluid into the channel through a circular hole on the bottom. As time progresses, the lighter fluid rises towards the upper boundary of the channel, overturning to form a mushroom-shaped profile as it moves. Details of the Boussinesq viscous flow model are presented in Section 2. Its great simplifying feature is that it replaces the mathematical interface, across which quantities such as density may jump discontinuously, with an “interfacial region” of finite width, in which density varies smoothly from one fluid to the other. A novel spectral method is used to solve this problem, and relies on first creating a suitable “background flow” and density profile that satisfy exactly the boundary conditions on the floor and ceiling of the channel, but not necessarily the viscous equations of motion in the fluid in between. This is achieved here assuming an irrotational flow from the circular hole on the channel bottom, which permits an exact solution using Hankel transforms. Details of this background flow and density are given in Section 3. This then forms the basis for the spectral solution method of Section 4. Results both for “lazy” and momentum-driven plumes are discussed in Section 5. The concluding Section 6 discusses the results and comments further on this spectral approach.

2. The Boussinesq fluid flow model

We consider a two-fluid system confined between two impermeable horizontal plates, with the z -axis pointing vertically and the gravitational body force per unit

mass, $-g\mathbf{e}_z$, directed downwards. The gravitational acceleration g is a constant, and the notation \mathbf{e}_z represents a unit vector in the direction of the positive z -axis. The bottom of the channel lies on the plane $z = 0$ and the top surface is at $z = H$. There is a circular hole of radius a in the bottom plate, with its centre on the z -axis, through which an incompressible fluid is injected with some maximum vertical speed $w_0/(2\pi)$. The fluid already present in the channel is referred to as Fluid 2, and it has constant density ρ_2 . The fluid injected through the hole in the bottom has density ρ_1 , and is referred to as Fluid 1. At the initial time $t = 0$, it is convenient to suppose that lower Fluid 1 forms a hemisphere of radius a centred on the origin of the coordinate system, and the key task of this investigation is to determine how the interfacial zone between the two fluids will evolve as time progresses.

It is convenient here to introduce dimensionless quantities, in which the radius a of the inlet hole is used as the reference length, and speeds are referred to the quantity \sqrt{ga} . The scale for all times is $\sqrt{a/g}$. The quantity ρ_1 is taken as the reference density. In these new dimensionless variables, the source hole in the bottom plate now has radius 1 and ejects fluid with nondimensional vertical speed $F/(2\pi)$, in which the constant

$$F = w_0/\sqrt{ga} \quad (2.1)$$

is a Froude number. Physically, F is a measure of the volume flux produced by the source, since if \mathbf{q} denotes the fluid velocity vector and \mathbf{n} is the upward normal to the bottom,

$$\iint \mathbf{q} \cdot \mathbf{n} \, dS = \int_0^{2\pi} \int_0^1 \mathbf{q} \cdot \mathbf{nr} \, dr \, d\theta = \frac{1}{2}F, \quad (2.2)$$

which is the volume flux over half a sphere of unit radius.

In addition to the Froude number in (2.1), there are four more possible dimensionless parameters needed to describe solutions to this problem. These are

$$h = \frac{H}{a}, \quad \frac{1}{R_e} = \frac{\mu_1}{\rho_1 \sqrt{a^3 g}}, \quad K_\sigma = \frac{\sigma}{\sqrt{a^3 g}}, \quad D = \frac{\rho_2}{\rho_1}. \quad (2.3)$$

The first of these, h , is the dimensionless height of the channel, and R_e is a Reynolds number, based on the viscosity μ_1 and density ρ_1 of the lower injected fluid, although for simplicity both fluids here will be assumed to have the same viscosity. Parameter K_σ is a density-diffusion coefficient that is sometimes introduced in the Boussinesq formulation, and σ is its dimensional counterpart. It is related to a Prandtl number (see the article by Farrow and Hocking [9]). Parameter D is the density ratio of upper Fluid 2 to lower Fluid 1. A sketch of the flow geometry here, in dimensionless variables, is given in Figure 1. We observe that if buoyancy were to be taken into account in the definition of the Froude number, then the gravitational acceleration g in our definition (2.1) above could be replaced with the reduced gravity $g(\rho_2 - \rho_1)/\rho_2$ to define an alternative Froude number $F_B = F\sqrt{D/(D-1)}$. In this paper, however, we will refer only to the parameters F and D , since each corresponds to just a single physical effect.

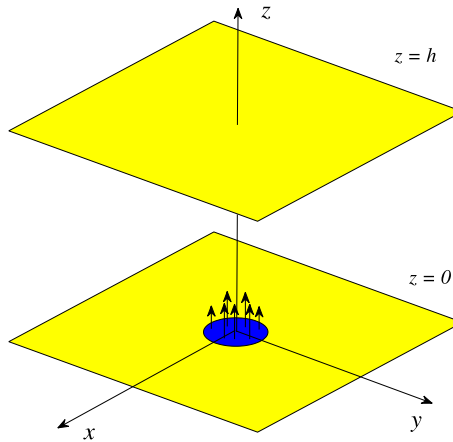


FIGURE 1. A schematic diagram of the flow configuration in dimensionless variables.

In the Boussinesq formulation used here, it is assumed that variations in the density ρ are small, and that density varies smoothly and continuously between the two fluid layers, rather than jumping discontinuously at an interface between them. Physically, this corresponds to the sharp interface being replaced with a narrow interfacial zone in which mixing of the two fluids occurs. Thus, Boussinesq theory assumes that the density everywhere in the fluid is some small quantity $\bar{\rho}$ above the density of injected Fluid 1, so that

$$\rho(x, y, z, t) = 1 + \bar{\rho}(x, y, z, t).$$

The compressible continuity equation, expressing conservation of mass within the fluid, is then typically “split” into an incompressible part

$$\text{div } \mathbf{q} = 0 \tag{2.4}$$

and a weakly compressible transport equation

$$\frac{\partial \bar{\rho}}{\partial t} + \mathbf{q} \cdot \nabla \bar{\rho} = K_\sigma \nabla^2 \bar{\rho} \tag{2.5}$$

for the convection and possible diffusion of the density perturbation function $\bar{\rho}$. The diffusion constant K_σ is defined in equation (2.3) above. As discussed by Forbes [13], the quantity $\bar{\rho}$ could also be regarded as a temperature perturbation, or even a salinity concentration, in the Boussinesq approach.

In dimensionless form, the Boussinesq form of the Navier–Stokes equation, that expresses conservation of linear momentum, becomes

$$\frac{\partial \mathbf{q}}{\partial t} + (\mathbf{q} \cdot \nabla) \mathbf{q} + \nabla p = -(1 + \bar{\rho}) \mathbf{e}_z + \frac{1}{Re} \nabla^2 \mathbf{q}. \tag{2.6}$$

A key quantity, too, is the vorticity vector $\boldsymbol{\zeta} = \nabla \times \mathbf{q}$, which represents twice the local angular velocity. It is convenient to take the curl of the entire Navier–Stokes equation

(2.6), since this eliminates the term involving the pressure p , which is difficult to compute. This gives rise to a vorticity equation in the general form

$$\frac{\partial \zeta}{\partial t} + (\mathbf{q} \cdot \nabla) \zeta - (\zeta \cdot \nabla) \mathbf{q} = -\nabla \times (\bar{\rho} \mathbf{e}_z) + \frac{1}{R_e} \nabla^2 \zeta. \quad (2.7)$$

It is appropriate now to transform to cylindrical polar coordinates (r, θ, z) for this circularly cylindrical flow. This is accomplished by means of the usual relations $x = r \cos \theta$, $y = r \sin \theta$, with z remaining unchanged. This introduces the nonconstant unit basis vectors $\mathbf{e}_r = \cos \theta \mathbf{e}_x + \sin \theta \mathbf{e}_y$ and $\mathbf{e}_\theta = -\sin \theta \mathbf{e}_x + \cos \theta \mathbf{e}_y$ pointing in the positive radial and azimuthal directions, respectively. The fluid velocity vector \mathbf{q} is expressed as $\mathbf{q} = u \mathbf{e}_r + v \mathbf{e}_\theta + w \mathbf{e}_z$. Because the flow is axisymmetric, there is no θ -dependence. In addition, we suppose that there is no azimuthal swirl component of the velocity vector, so that $v = 0$. In polar coordinates, the incompressibility condition (2.4) becomes

$$\frac{1}{r} \frac{\partial}{\partial r} (ru) + \frac{\partial w}{\partial z} = 0 \quad (2.8)$$

and the transport equation (2.5) takes the form

$$\frac{\partial \bar{\rho}}{\partial t} + u \frac{\partial \bar{\rho}}{\partial r} + w \frac{\partial \bar{\rho}}{\partial z} = K_\sigma \left[\frac{1}{r} \frac{\partial}{\partial r} \left(r \frac{\partial \bar{\rho}}{\partial r} \right) + \frac{\partial^2 \bar{\rho}}{\partial z^2} \right]. \quad (2.9)$$

Since the flow is axisymmetric, with $v = 0$, it follows that the vorticity vector ζ has only a single component in the azimuthal direction, so that

$$\zeta = \zeta \mathbf{e}_\theta \quad \text{with} \quad \zeta = - \left[\frac{\partial w}{\partial r} - \frac{\partial u}{\partial z} \right]. \quad (2.10)$$

After some algebra, this gives the polar form of the vorticity equation (2.7) to be

$$\frac{\partial \zeta}{\partial t} + u \frac{\partial \zeta}{\partial r} + w \frac{\partial \zeta}{\partial z} - \frac{u \zeta}{r} = \frac{\partial \bar{\rho}}{\partial r} + \frac{1}{R_e} \left[\frac{1}{r} \frac{\partial}{\partial r} \left(r \frac{\partial \zeta}{\partial r} \right) + \frac{\partial^2 \zeta}{\partial z^2} - \frac{\zeta}{r^2} \right] \quad (2.11)$$

in terms of the single scalar component ζ in equation (2.10).

The polar form (2.8) of the continuity equation can be solved identically using a streamfunction $\Psi(r, z, t)$, from which the velocity components u and w are then calculated according to the relations

$$u = -\frac{\partial \Psi}{\partial z} \quad \text{and} \quad w = \frac{1}{r} \frac{\partial}{\partial r} (r \Psi), \quad (2.12)$$

as explained in [6, p. 78]. At least for steady flow, it is possible to show that the quantity $r\Psi$ is constant along a streamline. It follows from (2.10) that the vorticity ζ may be expressed directly in terms of the streamfunction Ψ according to the relation

$$\zeta = - \left[\frac{1}{r} \frac{\partial}{\partial r} \left(r \frac{\partial \Psi}{\partial r} \right) + \frac{\partial^2 \Psi}{\partial z^2} - \frac{\Psi}{r^2} \right]. \quad (2.13)$$

Thus, a solution to this nonlinear Boussinesq problem consists of finding the function $\Psi(r, z, t)$, from which velocity components and vorticity can be computed from

equations (2.12) and (2.13), along with the function $\bar{\rho}(r, z, t)$, such that the transport equation (2.9) and the vorticity equation (2.11) are satisfied. In this paper, we ignore the narrow boundary layers on the top and bottom plates, which is equivalent to allowing fluid slip to take place at these boundaries (or, equivalently, slip can be thought of as occurring at the edges of these very narrow boundary layers). On the top plate,

$$w = 0 \quad \text{and} \quad \zeta = 0 \quad \text{at} \quad z = h. \quad (2.14)$$

At the bottom of the fluid channel,

$$w = w_{b0}(r) \quad \text{and} \quad \zeta = 0 \quad \text{at} \quad z = 0, \quad (2.15)$$

where the vertical input speed $w_{b0}(r)$ is chosen to specify conditions at the inlet and across the rest of the plate. An obvious simple choice might be the discontinuous function

$$w_{b0}(r) = \begin{cases} F/(2\pi) & \text{if } 0 < r < 1, \\ 0 & \text{if } r > 1, \end{cases}$$

in which the Froude number F is chosen to be consistent with the input flux of lower Fluid 1, according to (2.1) and (2.2). However, a careful analysis of the background flow generated by a discontinuous vertical velocity profile such as this reveals that the solution fails to converge to the degree of differentiability required. Accordingly, continuous and smooth velocity and density profiles must be specified at the bottom boundary $z = 0$, as is discussed next in Section 3.

3. Inviscid background source flow

In this section, we create an inviscid (nonviscous) flow of an incompressible fluid, which satisfies exactly the boundary conditions (2.14) and (2.15). Of course, this inviscid solution does not satisfy the viscous-Boussinesq equations of Section 2, but can be used as a framework on which a viscous solution can be constructed later.

We take this background configuration to be an irrotational flow of an inviscid fluid and hence it can be constructed with the aid of a velocity potential $\Phi(r, z)$. This scalar function satisfies Laplace's equation

$$\nabla^2 \Phi = \frac{1}{r} \frac{\partial}{\partial r} \left(r \frac{\partial \Phi}{\partial r} \right) + \frac{\partial^2 \Phi}{\partial z^2} = 0. \quad (3.1)$$

The background velocity vector \mathbf{q}_B is obtained from $\mathbf{q}_B = \nabla \Phi$, and the condition (2.14) demands that

$$\partial \Phi / \partial z = 0 \quad \text{at} \quad z = h. \quad (3.2)$$

A solution to Laplace's equation (3.1) is sought as a Hankel transform of order zero, in the form

$$\Phi(r, z) = \int_0^\infty H(k; z) J_0(kr) dk, \quad (3.3)$$

in which $J_0(z)$ denotes the Bessel function of the first kind of order 0. In order to satisfy Laplace's equation (3.1), it is necessary to choose

$$H(k; z) = C(k) \frac{\cosh(k(h - z))}{\sinh(kh)}$$

in the integrand of the expression (3.3). This choice also satisfies the condition (3.2) of no flow across the top boundary of the channel. The solution therefore becomes

$$\Phi(r, z) = \int_0^\infty C(k) \frac{\cosh(k(h - z))}{\sinh(kh)} J_0(kr) dk. \tag{3.4}$$

It still remains to impose the vertical component of fluid speed along the bottom plane $z = 0$ of the fluid channel, according to the condition (2.15). Combined with (3.4) this gives

$$\frac{\partial \Phi}{\partial z}(r, 0) = w_{b0} = - \int_0^\infty kC(k)J_0(kr) dk,$$

which is an integral equation for the function $C(k)$. The solution is obtained at once using the inverse Hankel transform, and yields

$$C(k) = - \int_0^\infty r w_{b0}(r) J_0(kr) dr. \tag{3.5}$$

It remains now to specify the desired form of the vertical speed at the bottom $z = 0$. We seek a function that is continuous along with its first two derivatives, zero over the actual bottom $r > 1$ of the channel but positive over the location $0 < r < 1$ of the input pipe, and having a zero derivative at $r = 0$. After some experimentation, it was decided to adopt the cubic-spline function in r^2 given simply as

$$w_{b0}(r) = \begin{cases} (2F/\pi)(1 - r^2)^3 & \text{if } 0 < r < 1, \\ 0 & \text{if } r > 1, \end{cases} \tag{3.6}$$

which satisfies the inlet flux condition (2.2). From equation (3.5), it follows that the term $C(k)$ in the solution (3.4) is, therefore, given by the expression

$$C(k) = - \frac{2F}{\pi} \int_0^1 r(1 - r^2)^3 J_0(kr) dr.$$

Upon making the change of variable $Z = kr$, this expression becomes

$$C(k) = - \frac{2F}{\pi k} \int_0^k \left[\frac{Z}{k} - 3 \frac{Z^3}{k^3} + 3 \frac{Z^5}{k^5} - \frac{Z^7}{k^7} \right] J_0(Z) dZ. \tag{3.7}$$

It turns out that these integrals can be evaluated in closed form, using repeated integration by parts and the indefinite integral

$$\int Z^{p+1} J_p(Z) dZ = Z^{p+1} J_{p+1}(Z)$$

from Gradshteyn and Ryzhik [15, p. 624]. After some algebra,

$$\begin{aligned} \int Z J_0(Z) dZ &= Z J_1(Z), \\ \int Z^3 J_0(Z) dZ &= Z^3 J_1(Z) - 2Z^2 J_2(Z), \\ \int Z^5 J_0(Z) dZ &= Z^5 J_1(Z) - 4Z^4 J_2(Z) + 8Z^3 J_3(Z), \\ \int Z^7 J_0(Z) dZ &= Z^7 J_1(Z) - 6Z^6 J_2(Z) + 24Z^5 J_3(Z) - 48Z^4 J_4(Z). \end{aligned} \tag{3.8}$$

These results are used in the evaluation of the integral (3.7) and eventually give the simple outcome

$$C(k) = -\frac{96F}{\pi} \frac{J_4(k)}{k^4}. \tag{3.9}$$

The velocity potential Φ is now given by (3.4).

The components of the fluid velocity vector \mathbf{q}_B for this background flow are obtained from (3.4) by straightforward differentiation. They are

$$\begin{aligned} u_B(r, z) &= -\int_0^\infty kC(k) \frac{\cosh(k(h-z))}{\sinh(kh)} J_1(kr) dk, \\ w_B(r, z) &= -\int_0^\infty kC(k) \frac{\sinh(k(h-z))}{\sinh(kh)} J_0(kr) dk. \end{aligned} \tag{3.10}$$

These will be used in Section 4 as background flow for the full viscous solution technique. The vorticity for this background flow is zero.

The streamfunction $\Psi_B(r, z)$ can also be created for this background flow, using the velocity components (3.10) and the definition equations (2.12). After a little algebra, and making use of recurrence relations for the Bessel functions [1, p. 361],

$$\Psi_B(r, z) = -\int_0^\infty C(k) \frac{\sinh(k(h-z))}{\sinh(kh)} J_1(kr) dk. \tag{3.11}$$

These expressions (3.10) and (3.11) for the velocity components and streamfunction are highly convergent, since the kernel function $C(k)$ in (3.9) is finite at $k = 0$ and decays rapidly as $k \rightarrow \infty$.

In addition to the background fluid velocity field (3.10) and (3.11) created here, it is also necessary to derive a background density profile, so that the presence of the less-dense input Fluid 1 can be maintained across the inlet hole. To achieve this, we choose a representation

$$\bar{\rho}_B(r, z) = (D - 1) + \int_0^\infty kB(k) \frac{\sinh(k(h-z))}{\sinh(kh)} J_0(kr) dk. \tag{3.12}$$

We want the background density on the bottom $z = 0$ to be continuous and have a continuous first derivative. It should take the value $(D - 1)$ for Fluid 2 in the region

$r > 1$ outside the inlet pipe, and, for a region $0 < r < r_E$ inside the pipe, the perturbation density should simply have the value $\bar{\rho}_B = 0$, appropriate for Fluid 1. There would also be an edge region $r_E < r < 1$ inside the pipe, where the two fluids mix and the density transitions smoothly from one fluid to the other. Thus,

$$\bar{\rho}_B(r, z) = (D - 1) + \begin{cases} -(D - 1) & \text{if } 0 < r < r_E, \\ (D - 1)\mathcal{R}(r) & \text{if } r_E < r < 1, \\ 0 & \text{if } r > 1, \end{cases} \tag{3.13}$$

with the transition function in the edge region taken to be

$$\mathcal{R}(r) = -3 \frac{(1 - r^2)^2}{(1 - r_E^2)^2} + 2 \frac{(1 - r^2)^3}{(1 - r_E^2)^3}. \tag{3.14}$$

When the Hankel transform representation (3.12) of the density is evaluated on the bottom $z = 0$ and set equal to the specified function (3.13), an integral equation is again obtained for the unknown kernel function $B(k)$. It may be solved using the inverse Hankel transform, as previously for equation (3.5), so that

$$B(k) = -(D - 1) \int_0^{r_E} r J_0(kr) dr + (D - 1) \int_{r_E}^1 r \mathcal{R}(r) J_0(kr) dr.$$

The integrals in this expression may again be evaluated using the identities (3.8). After a considerable calculation, the required kernel function turns out to be

$$B(k) = (D - 1) \left[-\frac{24}{(1 - r_E^2)^2} \frac{\{J_3(k) + r_E^3 J_3(kr_E)\}}{k^3} + \frac{96}{(1 - r_E^2)^3} \frac{\{J_4(k) - r_E^4 J_4(kr_E)\}}{k^4} \right]. \tag{3.15}$$

The perturbation density $\bar{\rho}_B$ for this background configuration can now be calculated using the Hankel representation (3.12), and converges well, since the kernel function $B(k)$ in equation (3.15) is well behaved at $k = 0$ and decreases rapidly as $k \rightarrow \infty$. In addition, the two spatial derivatives of the density function (3.12) can be obtained by direct differentiation of this expression, and also converge well.

While integrals such as (3.10), (3.11) and (3.12) and their spatial derivatives cannot be evaluated in closed form, they are nevertheless obtained numerically to a high degree of accuracy, using the Gauss–Legendre quadrature routine written by von Winckel [35]. In the spectral method to follow in Section 4, these integral functions are calculated once at the beginning of the computer algorithm, and their values are then stored in matrices that are simply looked up later as needed. As a consequence, there is no major effect on the overall run time of the numerical method from using these sophisticated functions to establish background conditions for the nonlinear flow.

An example of a background perturbation density function $\bar{\rho}_B$ is illustrated in Figure 2 for a density ratio $D = 1.1$. Thus, $\bar{\rho}_B = 0$ inside the inflow pipe, over $0 < r < r_E$, and $\bar{\rho}_B = (D - 1) = 0.1$ far away. Some very small Gibbs’ phenomenon oscillations [33, Ch. 2] might be visible along the plane $z = 0$, but these are too small

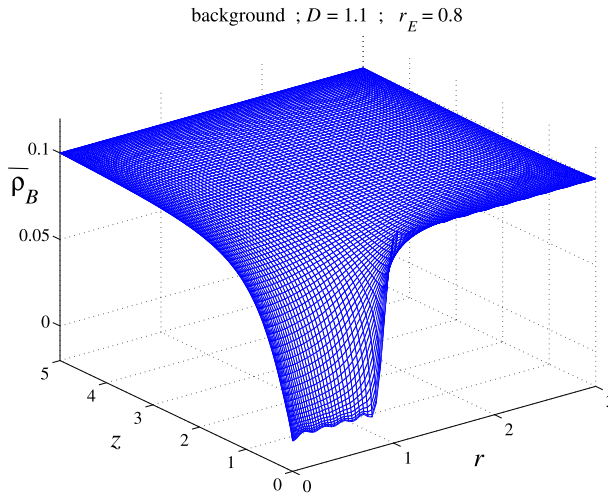


FIGURE 2. A representative background density profile, for a channel of height $h = 5$, with edge radius $r_E = 0.8$ and density ratio $D = 1.1$. Here, the computational window is $R_\infty = 3$.

to be of consequence. They can be made to vanish using a smaller value of the edge radius $r_E = 0.8$ than illustrated here, but this brings the cost of a more diffuse interface for the density. Various types of smoothing could also be employed, but that has not been found necessary here. The use of a background density such as that in Figure 2 enforces the lower density of Fluid 1 at the inlet hole on the bottom.

4. The spectral solution method

A solution is now sought for the Boussinesq viscous plume described in Section 2. Spectral methods have the appeal that they can converge extremely rapidly with respect to the number of modes used (see the book by Boyd [7]), derivatives can be calculated to very high accuracy directly from the assumed forms of the variables and the Poisson equation (2.13) that relates the vorticity ζ and the streamfunction Ψ can be solved exactly for that number of modes, requiring no numerical approximation or iteration schemes. Furthermore, terms such as ζ/r^2 in equation (2.11), that may have a coordinate singularity at $r = 0$, can often be accounted for exactly by a judicious choice of basis function in the spectral representation of the solution. Accordingly, the problem stated in Section 2 will be solved here using a semi-analytical representation of the flow variables, in a spectral formulation.

The streamfunction $\Psi(r, z, t)$ is expressed by means of the series

$$\Psi(r, z, t) = \Psi_B(r, z) + \sum_{m=1}^M \sum_{n=1}^N A_{mn}(t) J_1(\alpha_m r) \sin(n\pi z/h). \quad (4.1)$$

Here, the function $\Psi_B(r, z)$ is the streamfunction developed in Section 3 for the steady-state background flow, given by (3.11), and the aim here is to find the unknown

Fourier–Bessel coefficients $A_{mn}(t)$. For numerical purposes, a “computational window” $0 < r < R_\infty$ is assumed, in which the constant R_∞ is assumed to be sufficiently large as not to interfere with the developing plume, over the time intervals of interest. The quantities

$$\alpha_m = j_{1,m}/R_\infty \quad (4.2)$$

are given in terms of the positive zeros $j_{1,m}$ of the J_1 Bessel function of the first kind and first order, and the two sums in the representation (4.1) are necessarily terminated at finite orders M and N , as indicated. It follows from the defining equations (2.12) for the streamfunction that the two velocity components u and w in the radial and vertical directions can be obtained at once from (4.1), and become

$$\begin{aligned} u(r, z, t) &= u_B(r, z) - \sum_{m=1}^M \sum_{n=1}^N A_{mn}(t)(n\pi/h)J_1(\alpha_m r) \cos(n\pi z/h), \\ w(r, z, t) &= w_B(r, z) + \sum_{m=1}^M \sum_{n=1}^N A_{mn}(t)\alpha_m J_0(\alpha_m r) \sin(n\pi z/h) \end{aligned}$$

in this spectral representation. The two velocity components u_B and w_B for the background flow are obtained from (3.10). Similarly, the vorticity ζ is obtained from (2.13) and (4.1) and is given by

$$\zeta(r, z, t) = \sum_{m=1}^M \sum_{n=1}^N K_{mn}^2 A_{mn}(t) J_1(\alpha_m r) \sin(n\pi z/h), \quad (4.3)$$

without further approximation, where constants

$$K_{mn}^2 = \alpha_m^2 + (n\pi/h)^2 \quad (4.4)$$

have been defined for convenience. Since the background flow in Section 3 was taken to be irrotational, there is consequently no background term in the expression (4.3) for the nonlinear vorticity.

A similar spectral representation is also needed for the density perturbation $\bar{\rho}$. This function is required to maintain compatibility with the streamfunction (4.1) in the vorticity equation (2.11). Since the background density function $\bar{\rho}_B$ in equation (3.12) already accounts exactly for the boundary conditions on the upper and lower surfaces of the channel, it is sufficient to take

$$\bar{\rho}(r, z, t) = \bar{\rho}_B(r, z) + \sum_{m=1}^M \sum_{n=1}^N B_{mn}(t) J_0(\alpha_m r) \sin(n\pi z/h). \quad (4.5)$$

The constants α_m are as defined in (4.2) and involve the zeros of the J_1 Bessel function.

These spectral forms (4.3) and (4.5) are substituted into the linear terms in the vorticity equation (2.11), but the nonlinear convective terms are simply left in their

present form. The resulting equation is then multiplied by $rJ_1(\alpha_k r)$ and integrated over the domain $0 < r < R_\infty$, making use of the orthogonality result

$$\int_0^{R_\infty} rJ_1(\alpha_m r)J_1(\alpha_k r) dr = \begin{cases} 0 & \text{if } m \neq k, \\ (1/2)R_\infty^2 J_0^2(\alpha_k R_\infty) & \text{if } m = k. \end{cases} \tag{4.6}$$

This may be derived from a formula given in Abramowitz and Stegun [1, formula (11.4.5), p. 485]. Next, the system is multiplied by $\sin(\ell\pi z/h)$ and integrated over $0 < z < h$, using the standard orthogonality condition for the sine function over a half period [1, p. 78]. This results in a system of ordinary differential equations for the Fourier coefficients $A_{k\ell}$, which may be written as

$$\begin{aligned} A'_{k\ell}(t) = & -\frac{1}{R_e} K_{k\ell}^2 A_{k\ell}(t) - \frac{\alpha_k}{K_{k\ell}^2} B_{k\ell}(t) \\ & - \frac{4}{hK_{k\ell}^2 W_k^2} \int_0^h \int_0^{R_\infty} \left[ru \frac{\partial \zeta}{\partial r} + rw \frac{\partial \zeta}{\partial z} - u\zeta - r \frac{\partial \bar{\rho}_B}{\partial r} \right] J_1(\alpha_k r) \sin(\ell\pi z/h) dr dz, \\ & k = 1, 2, \dots, M, \ell = 1, 2, \dots, N. \end{aligned} \tag{4.7}$$

In this expression, we define constants

$$W_k = R_\infty J_0(\alpha_k R_\infty). \tag{4.8}$$

The transport equation (2.9) is similarly subjected to Fourier analysis, to derive a system of ordinary differential equations for the coefficients $B_{m\ell}(t)$ in the representation (4.5) of the density perturbation function $\bar{\rho}$. The spectral series are substituted directly into the linear terms in (2.9) and, since the background density function $\bar{\rho}_B$ in (3.12) was defined as a solution of Laplace’s equation, it cancels in the diffusion term on the right-hand side of equation (2.9). The equation is again multiplied by $rJ_0(\alpha_k r)$ and integrated over the interval $0 < r < R_\infty$. We use the appropriate orthogonality relation for the J_0 Bessel function [1, p. 485], which in fact gives precisely the same result as for the J_1 Bessel function in (4.6). This is because of the relationship $J'_0(z) = -J_1(z)$. Next, the system is again multiplied by basis functions $\sin(\ell\pi z/h)$ and integrated over $0 < z < h$, using the trigonometric orthogonality relations. This gives the further system of differential equations

$$\begin{aligned} B'_{k\ell}(t) = & -K_\sigma B_{k\ell}(t) K_{k\ell}^2 \\ & - \frac{4}{hW_k^2} \int_0^h \int_0^{R_\infty} r \left(u \frac{\partial \bar{\rho}}{\partial r} + w \frac{\partial \bar{\rho}}{\partial z} \right) J_0(\alpha_k r) \sin(\ell\pi z/h) dr dz, \\ & k = 1, 2, \dots, M, \ell = 1, 2, \dots, N. \end{aligned} \tag{4.9}$$

Here, the constants $K_{k\ell}^2$ are as defined in equation (4.4) and the W_k are defined in (4.8).

Equations (4.7) and (4.9) constitute a system of $2MN$ ordinary differential equations for the same number of Fourier coefficients in the representations (4.3) and (4.5) for the vorticity ζ and density perturbation $\bar{\rho}$. These are integrated forward in time using a

Runge–Kutta–Fehlberg method [3, p. 318]. To calculate the zeros $j_{1,m}$ of the Bessel J_1 function in (4.2), we used a simple bisection algorithm, since this was guaranteed to give the required zero as needed, and cannot jump to other roots of the function, as is possible with Newton’s method, for example. Nevertheless, Horsley [17] has recently devised an algorithm for zeros of Bessel-function cross-products, and those principles may be useful here, too. Numerical quadrature is also required in the evaluation of terms such as those in equations (4.7), and this is carried out to extremely high accuracy using the Gaussian-quadrature routine `lgwt` written by von Winckel [35]. The computer run time is reduced very substantially by calculating and storing the Bessel functions $J_0(\alpha_m r)$, $J_1(\alpha_m r)$ and even the trigonometric functions $\cos(n\pi z/h)$, $\sin(n\pi z/h)$. These are calculated once only at the beginning of the algorithm and stored in matrices of the appropriate sizes. Values of these functions at the mesh points are later retrieved from these matrices as required, without further calculation.

Initial conditions for the flow variables are required, in order to start the numerical solution. The velocity components u_B and w_B from the background flow (3.10) are appropriate starting speeds, and accordingly we simply set $A_{mn}(0) = 0$ for the coefficients in the representation of the vorticity (4.3).

For the initial density profile, we have chosen a hemisphere of dimensionless radius 1 centred at the origin and containing the lighter Fluid 1. The remainder of the channel is filled with the heavier outer Fluid 2. This would represent a bubble of the lighter Fluid 1 of the same diameter as the inlet pipe sitting above the pipe at the first instant. As with the bottom profile (3.13), we have also insisted that the initial density distribution and its first derivatives should be continuous and so we take

$$\bar{\rho}(r, z, 0) = (D - 1) + \begin{cases} -(D - 1) & \text{if } 0 < R_S < r_E, \\ (D - 1)\mathcal{R}(R_S) & \text{if } r_E < R_S < 1, \\ 0 & \text{if } R_S > 1, \end{cases} \quad (4.10)$$

with the same function $\mathcal{R}(r)$ as in equation (3.14), but now with argument given by the spherical radius function

$$R_S = \sqrt{r^2 + z^2}.$$

In this case, the initial coefficients are

$$B_{k\ell}(0) = \frac{4}{hW_k^2} \int_0^h \int_0^{R_\infty} r[\bar{\rho}(r, z, 0) - \bar{\rho}_B(r, z)]J_0(\alpha_k r) \sin(\ell\pi z/h) dr dz, \quad (4.11)$$

in which the functions W_k in the denominator are given by (4.8), as previously. The initial density profile (4.10) is inserted into this equation and the coefficients in (4.11) are evaluated numerically using the Gaussian quadrature code `lgwt` provided by von Winckel [35].

5. Presentation of results

5.1. A lazy plume We begin this presentation of sample results with a discussion of the so-called “lazy” plume [19], in which the morphology of the inflow is determined solely by buoyancy. There is thus no forced inflow, and we set $F = 0$ in (3.6). We choose a moderate Reynolds number $1/R_e = 10^{-3}$ and diffusion coefficient $K_\sigma = 10^{-4}$, and the edge parameter in the pipe is set to $r_E = 0.8$. The density ratio is set at the value $D = 1.1$. The lazy plume, with $F = 0$, turns out to be the most numerically sensitive of the situations studied here, and our tests indicate that, to maintain good accuracy over the time interval of results to be discussed here, it was necessary to take (at least) $M = N = 51$ Fourier coefficients and 201×201 mesh points over the domain defined by channel height $h = 5$ and (artificial) computational boundary $R_\infty = 3$. This is therefore a significant computational undertaking, and each such run required about 8 hours run time on a modern dual-core desktop computer, using the *MATLAB 2016a* programming environment. We have investigated the possibility of gaining significant reduction in run time, by re-coding the numerical scheme using *FORTRAN*, but this was not particularly successful, at least on a standard PC, when compared against *MATLAB 2016a* on the same machine. In order to be sure of the convergence of the numerical scheme, a small number of runs was also made using $M = N = 81$ Fourier coefficients and 201×201 mesh points over the fluid domain. This required about 28 hours run time. This gives very accurate results over the approximate dimensionless time interval $0 < t < 20$, and is illustrated in this section.

Figure 3 shows the rise of a lazy plume, with $D = 1.1$, so that the outer ambient Fluid 2 is 10% more dense than the inner Fluid 1 that is being introduced through the circular source hole. The channel height is $h = 5$. Solutions are shown at the six dimensionless times $t = 3, 7, 10, 13, 17$ and 20 . Here, contours of the density perturbation function $\bar{\rho}$ are shown, and have been filled for ease of viewing. The light-coloured zones correspond to regions of unmixed injected Fluid 1, for which $\bar{\rho} = 0$. These results were obtained using $M = N = 81$ Fourier coefficients. They agree very closely to calculations made with $M = N = 51$ coefficients, until about time $t = 12$. After that time, the less accurate results obtained with $M = N = 51$ continue to give a good overall description of the plume morphology, but cannot resolve the fine, delicate plume structures that form at later times, such as those presented here for $t = 13$ and $t = 17$. Further discussion of these numerical convergence issues is given in Section 6.

At the earliest time $t = 3$ shown in Figure 3, the region of light fluid still approximately occurs as a hemisphere, close to the initial condition (4.10), although the bottom portion has pulled inwards slightly from the rim of the injection hole at $r = 1$. By the next time $t = 7$, the plume has risen and is beginning to overturn, to form a mushroom-shaped structure. The plume continues to rise and overturn, and by time $t = 10$ it has formed a slender vertical stem and a pronounced overturning cap. By comparing the results in Figure 3 with those generated at different channel heights h , we can confirm that the plume at these earlier times is unaffected by the presence of the upper channel wall at $h = 5$. This theme will be returned to a little later. However, at the two last times shown in Figure 3, the top of the plume interacts with this upper

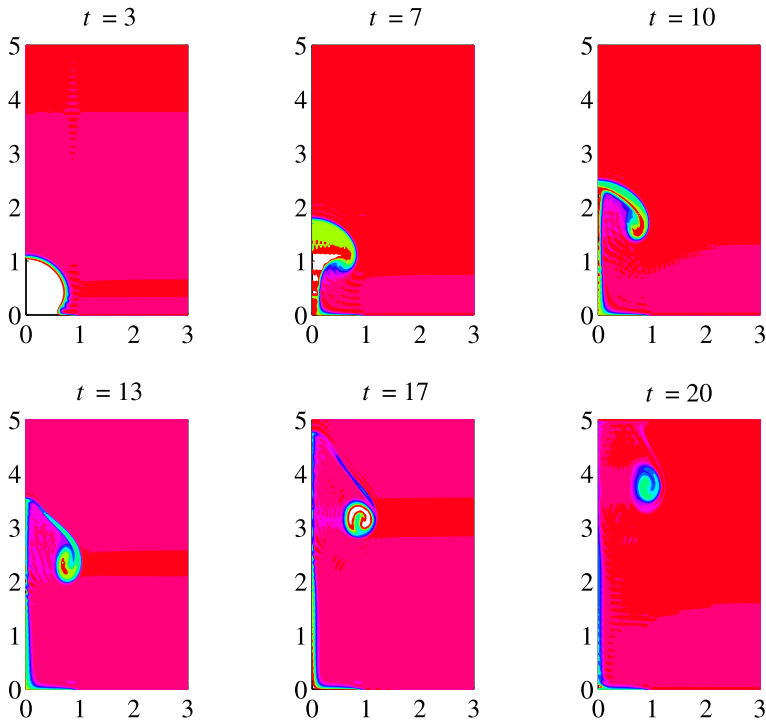


FIGURE 3. Density contours for a lazy plume at six different times as shown. The channel height is $h = 5$ and $D = 1.1$. Here, $R_\infty = 3$ and the scales on the axes are all equal. The coordinates r and z are plotted on the horizontal and vertical axes, respectively.

channel wall, hitting it and then spreading laterally. The plume cap is connected to the central stem at times $t = 13$ and $t = 17$, but has become a very slender and delicate structure. This is perhaps to be expected from a lazy plume that rises only under its own buoyancy. By the last time $t = 20$ shown in Figure 3, the plume cap has clearly broken, leaving a fine central stem and a separate ring vortex at the approximate height $z = 4$ above the channel bottom.

In Figure 4, we show contours of the function $r\Psi$ for the lazy plume presented in Figure 3, and for the same six times $t = 3, 7, 10, 13, 17$ and 20 . Streamlines are lines drawn in the fluid such that their tangent is everywhere parallel to the local velocity vector \mathbf{q} and, in cylindrical polar coordinates, it is straightforward to show that, at least for steady flow, these contours of $r\Psi$ are the streamlines. This is not necessarily so for unsteady flows like those discussed here, but these contours nevertheless provide at least an approximate guide to the streamline locations at each instant and hence give a broad description of the fluid motion.

At the earliest time $t = 3$ shown in Figure 4, it is clear that the upward motion of the fluid at the inlet hole, due purely to buoyancy, has created a ring vortex centred slightly inside the edge $r = 1$ of the inlet hole, at an elevation of about $z \approx 0.4$. This vortex is

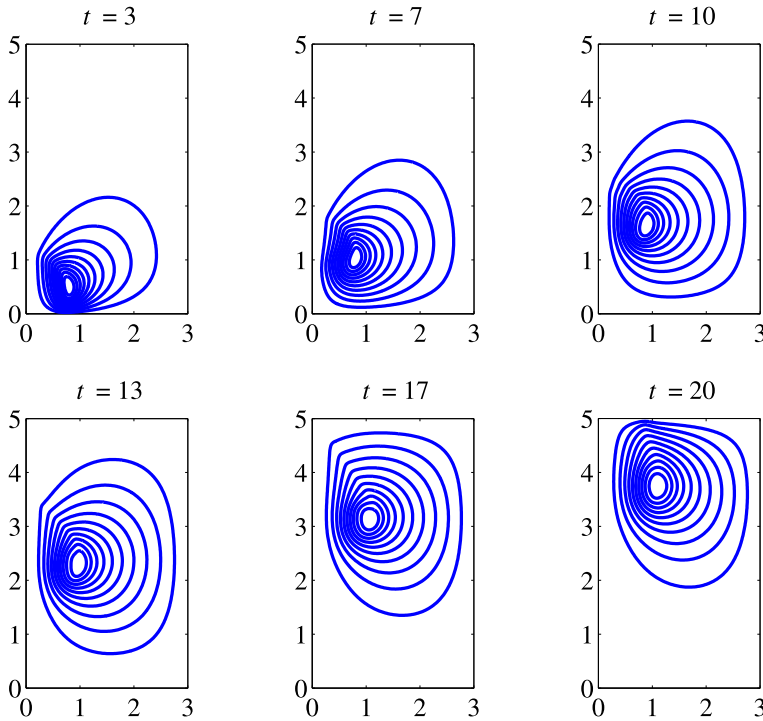


FIGURE 4. Instantaneous streamlines induced by the motion of the lazy plume in Figure 3 at the same six times shown. The channel height is $h = 5$ and $D = 1.1$. Here, $R_\infty = 3$ and the scales on the axes are all equal. The coordinates r and z are plotted on the horizontal and vertical axes, respectively.

associated with the overturning of the plume as depicted in Figure 3. At later times, the rising plume takes the vortex with it as it moves up the channel, so that by time $t = 7$ its centre is at height $z \approx 1$ and at time $t = 10$ the vortex centre has risen further to height $z \approx 1.7$. The vortex continues to rise until, at the last time $t = 20$ shown, the plume meets the upper wall at $z = h$ and the vortex ring begins to move outwards from the centreline. The scales on the vertical and horizontal axes are the same, as for Figure 3, so that this plume and its streamlines appear as they might be seen in reality.

As the lazy plume in Figure 3 rises due to its own buoyancy, it induces the formation of a ring vortex as a consequence of viscous entrainment, and the (approximate) streamlines in Figure 4 chronicle its evolution and motion. These considerations lead us naturally to consider how the vorticity ζ in (2.10) is induced by the plume and evolves with time. One advantage of the spectral method presented in Section 4 is that spatial derivatives of dependent variables can be evaluated to very high accuracy by explicit differentiation of the flow quantities, so that the expression (4.3) can be evaluated at once from the computed Fourier coefficients.

Contours of the vorticity $\zeta(r, z, t)$ are shown in Figure 5, again for the same flow discussed in Figures 3 and 4, and for the same six times $t = 3, 7, 10, 13, 17$ and 20 .

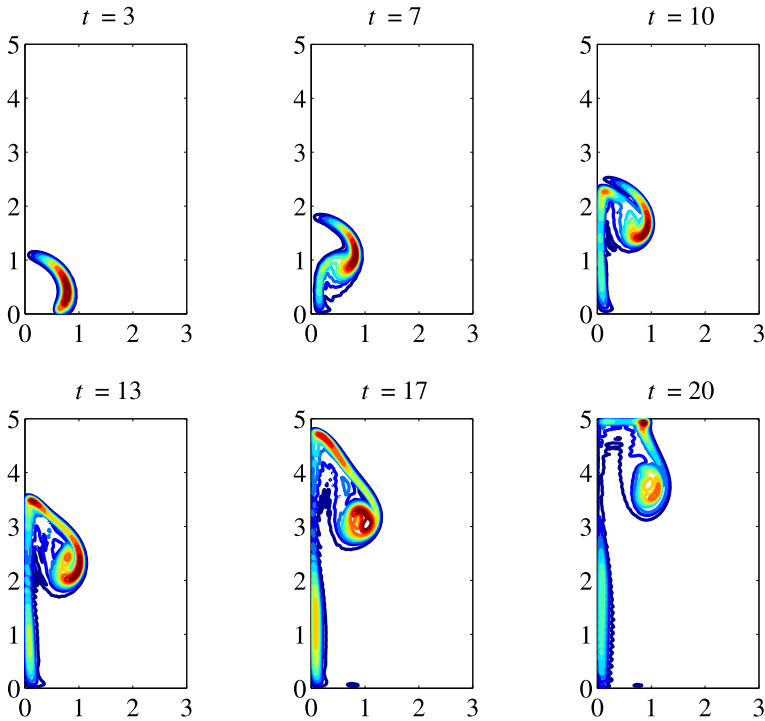


FIGURE 5. The vorticity induced in the fluid by the motion of the lazy plume in Figure 3 at the same six times shown. The channel height is $h = 5$ and $D = 1.1$. Here, $R_\infty = 3$ and the scales on the axes are all equal. The coordinates r and z are plotted on the horizontal and vertical axes, respectively.

It is interesting that the vorticity ζ calculated from the expression (4.3) is essentially zero over almost all the fluid region, so that these are almost irrotational flows. (This incidentally provides justification for the use of the irrotational background flow developed in Section 3.) At the earliest time $t = 3$ shown in Figure 5, the only vorticity that has been induced by the plume's motion occurs in the interfacial zone $r_E < \sqrt{r^2 + z^2} < 1$, where the density perturbation function $\bar{\rho}$ changes rapidly but smoothly. This is clearly visible in the diagram for $t = 3$, and mirrors closely the situation occurring with the Rayleigh–Taylor instability, as discussed by Forbes [10]. This induced vorticity at the interface is responsible for the plume overturning at later times. As time progresses, the vorticity remains largely confined to the moving interfacial zone, although there is some dissipation due to the combined effects of convection and diffusion in the governing equation (2.11). These influences are visible at later times. The interaction of the buoyant flow with the upper wall at the last time $t = 20$ shown in Figure 5 is particularly evident from that diagram. Although the flow has formed a separate vortex ring at about $z = 4$ at this time, there is nevertheless a patch of vorticity on the upper wall at about radius $r = 1$, in addition to the separate patch of vorticity in the detached ring.

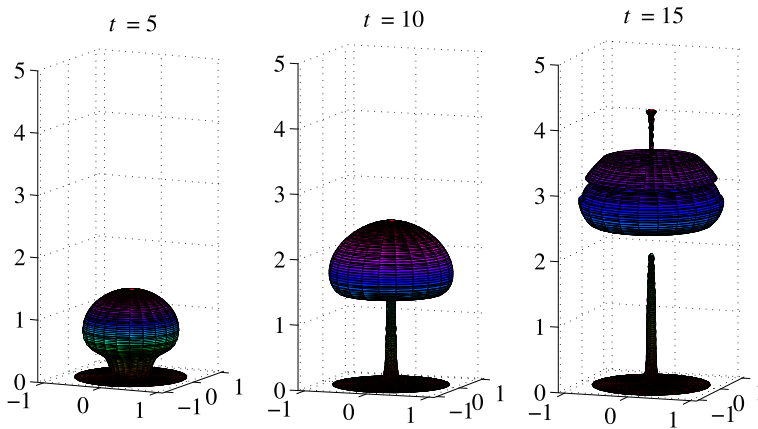


FIGURE 6. Approximate interface shapes for the lazy plume of Figure 3, but at the three different times $t = 5$, $t = 10$ and $t = 15$. The channel height is $h = 5$, $D = 1.1$ and $R_\infty = 3$. The scale on all three sets of axes is the same.

It is of interest to calculate the location of the “interface” between injected Fluid 1 and the ambient Fluid 2, and this is presented in Figure 6, for the same plume parameters as in Figures 3–5 in which $D = 1.1$, the channel height is $h = 5$ and the horizontal computational boundary is at $R_\infty = 3$ (and $F = 0$). In this Boussinesq theory, there is no true interface consisting of an infinitesimally thin surface across which the density jumps discontinuously and so an approximate interface location must be estimated from the numerical solution. For this particular solution, we were able to extract the density contour $\bar{\rho} = 0.04$ consistently from the numerical results, for each of the three times shown. Accordingly, this density contour was then rotated about the z -axis, to generate the three diagrams presented.

At time $t = 5$ shown in Figure 6, the original hemispherical interfacial zone $0.8 = r_E < \sqrt{r^2 + z^2} < 1$ in the initial condition (4.10) has drawn inwards near the bottom $z = 0$ but is beginning to overturn at about height $z \approx 0.5$. The next profile shown for time $t = 10$ may be compared with its density profile map presented in Figure 3 for that same time. By now, the upward movement of the induced vortex has left a very narrow stem of the lighter Fluid 1, connecting to the approximately spherical cap at about height $z \approx 2.4$. As this cap rises, it continues to overturn and, by time $t = 15$, it has detached from the central stem to form a couple of separate ring-vortex-type structures. The stem itself has also broken to create two separate blobs, with the upper one lying partially inside the vortex rings. It may be the case that for a fluid of unbounded height, or at least one for which h is very large, vortex rings like those shown for $t = 15$ might continue to form and detach, creating “smoke ring”-like structures at periodic intervals in the vertical coordinate z . It would require very much greater computer resources to investigate that speculation further, however.

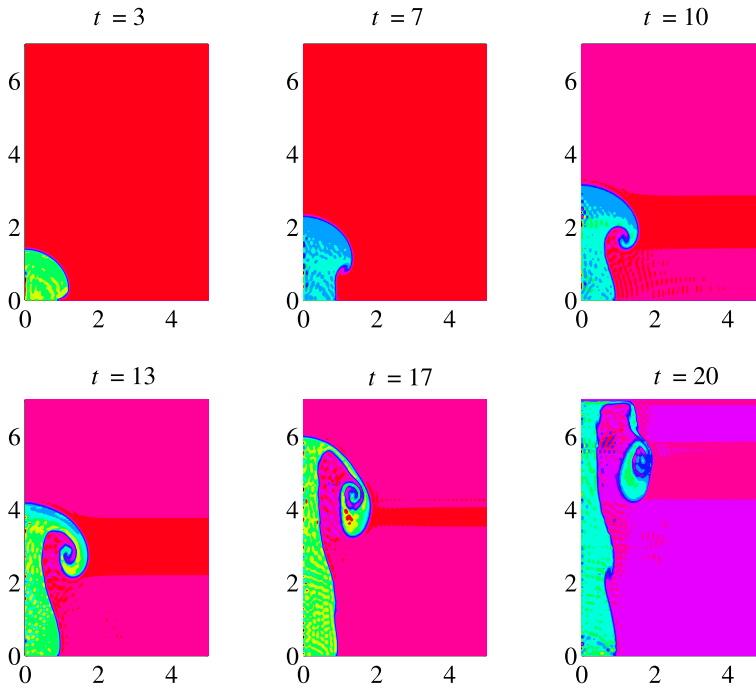


FIGURE 7. Density contours for a forced plume at the six different times shown. The channel height $h = 7$ and $D = 1.1$. Here, $R_\infty = 5$ and the scales on the axes are all equal. The coordinates r and z are plotted on the horizontal and vertical axes, respectively.

5.2. A forced plume We have also carried out a considerable number of computer runs in which the background forced flow (3.10) is present, with nonzero input Froude number F in (2.1). We illustrate these results in this section using the fixed Froude number $F = 2$ and using a very large, accurate calculation with $M = N = 81$ Fourier modes in the spectral method of Section 4.

Figure 7 gives density contours for a forced rising plume at the same six times $t = 3, 7, 10, 13, 17$ and 20 as for the lazy plume of Figures 3–5. The height of the channel has been increased to $h = 7$ and the computational window is extended out to radius $R_\infty = 5$. The density ratio is maintained at $D = 1.1$ and the input Froude number is $F = 2$. The results in Figure 7 are qualitatively similar to those in Figure 3 for the unforced plume, in the sense that both sets of results show first a perturbation to the initial hemisphere $\sqrt{r^2 + z^2} = 1$ of lighter Fluid 1, which then rises in a classical plume shape, with an axisymmetric stem connected to a bulbous head, which, at later times, overturns to form a mushroom-shaped outflow. There are, however, certain quantitative differences in morphology between the lazy and the forced plumes, and these are evident from a comparison of the two sets of diagrams. Perhaps the most obvious difference is the unsurprising observation that the forced plume rises more rapidly than its lazy counterpart, and this may be seen by comparing Figures 3 and 7 at

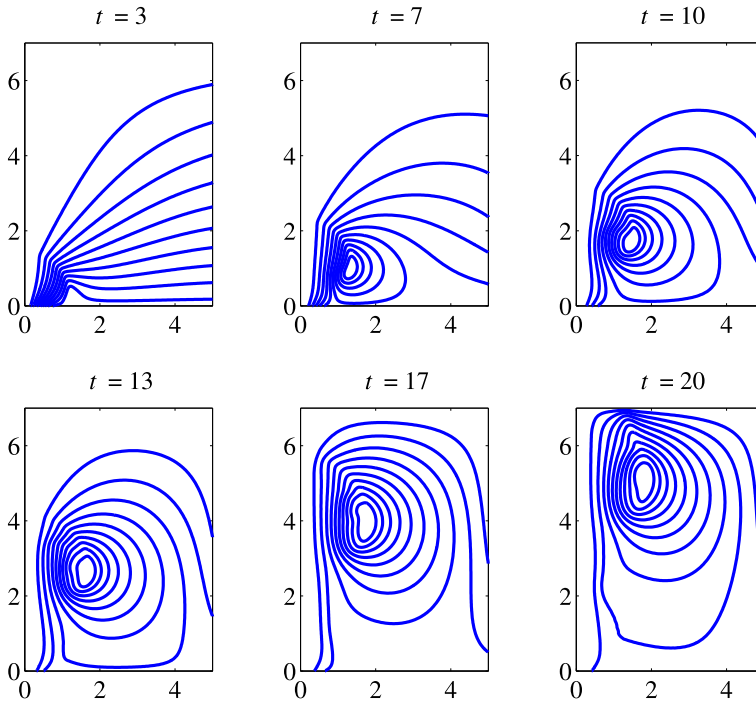


FIGURE 8. Streamlines for the forced plume illustrated in Figure 7 at the same six times shown. The channel height $h = 7$ and $D = 1.1$. Here, $R_\infty = 5$ and the scales on the axes are all equal. The coordinates r and z are plotted on the horizontal and vertical axes, respectively.

each of the six times shown. The other obvious difference in outflow morphologies is that, whereas the lazy plume in Figure 3 develops a very slender, delicate central stem connected to an overturning cap, the central stem for the forced plume in Figure 7 is much thicker. Again this is perhaps unsurprising, since the recharge rate of the light Fluid 1 across the inlet hole $r < 1$ on the bottom $z = 0$ is higher for the forced plume than for the lazy plume, in which recharge is only the result of buoyancy. By the time $t = 17$ illustrated in Figure 7 is attained, the plume cap has formed a tightly coiled overturned edge with at least two full turns. At the last time $t = 20$ shown in Figure 7, the plume cap has hit the top wall at $z = h$ and spread radially, so that the edge of the plume cap forms a coiled region with its centre at about radius $r = 2$. It appears, too, that a secondary overturning region may be about to form on the central stem, at approximate height $z \approx 2.3$.

Streamlines for this same case are illustrated in Figure 8 at the same six times $t = 3, 7, 10, 13, 17$ and 20 as shown in Figure 7. Again, these have been obtained using the representation (4.1), and plotting contours of the function $r\Psi$, since this function can easily be shown to be constant on streamlines, at least for steady flow. The contrast between this forced case and the streamlines for the unforced “lazy” plume shown in Figure 4 is striking. Since there is no forcing background flow for

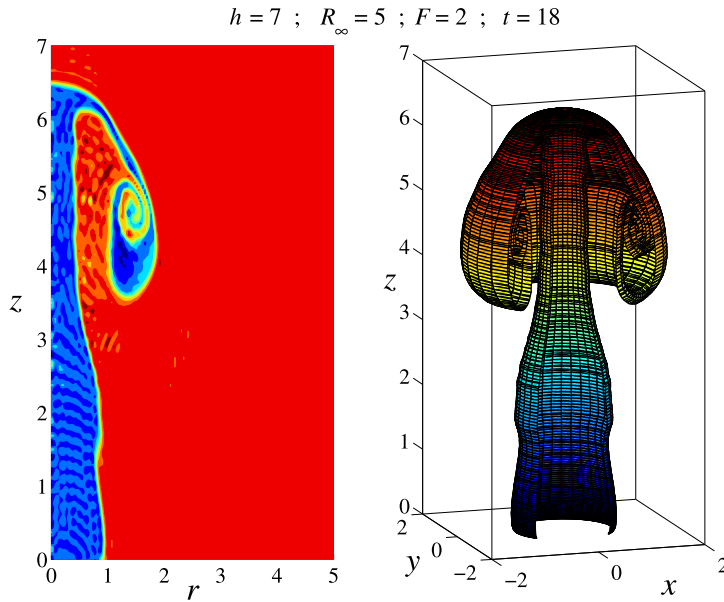


FIGURE 9. Two diagrams illustrating the rise of a forced plume at time $t = 18$. The left-hand picture is a contour map of the density perturbation $\bar{\rho}$. The image on the right is a cutaway diagram of the effective interface. The channel height $h = 7$ and Froude number $F = 2$. The scale is the same on all axes.

the lazy plume, the streamlines are induced entirely by the buoyant upwelling and so they occur as closed loops, corresponding to the natural formation of a ring vortex that surrounds the plume. By contrast, there is a background flow forcing the plume in Figure 8, for which the streamlines obtained from the solution (3.11) form surfaces that originate within the inlet hole $r < 1$ and then move upwards and outwards within the channel. Consequently, that streamline shape dominates the streamline pattern shown particularly in the first diagram in Figure 8 at the time $t = 3$. Nevertheless, the upward motion of the plume has also caused the formation of a small vortex region near the bottom of the tank, surrounding the plume and ultimately being responsible for plume overturning at later times, similarly to the lazy plume case illustrated in Figures 3 and 4. This vortex becomes evident by time $t = 7$ in the second diagram in Figure 8. At later times, it continues to gain in strength and to move upwards in the channel with the evolving plume. Since the plume is forced, lighter fluid continues to enter the channel through the hole on the bottom during the entire process. This is evident at the later times $t = 13, 17$ and 20 shown here, since streamlines continue to emanate from the hole on $z = 0$ over $0 < r < 1$, from which they enter the channel and eventually interact with the ring vortex.

In Figure 9, we present two images of the same forced plume as discussed in Figures 7 and 8, but now at time $t = 18$. The Froude number is $F = 2$, for a channel of height $h = 7$, and the computational boundary was set at $R_{\infty} = 5$. The image on the left

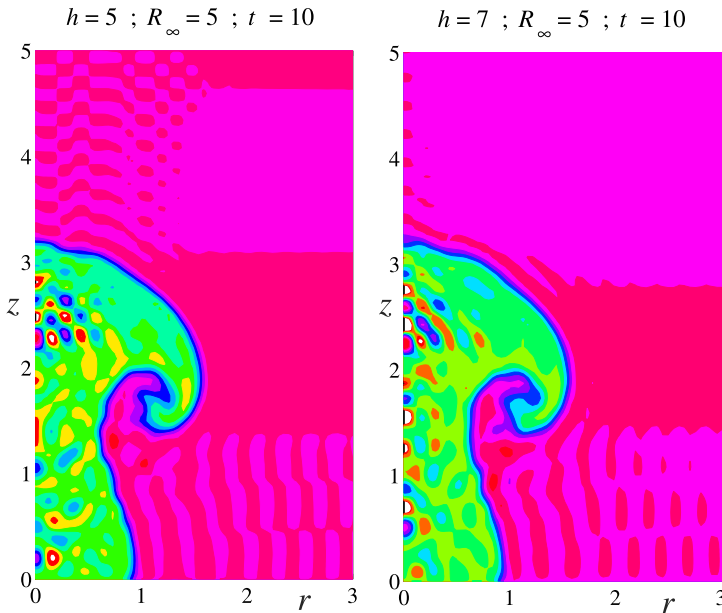


FIGURE 10. A comparison of two forced plumes at the same time $t = 10$, with $F = 2$ and $R_\infty = 5$, but in channels of two different heights $h = 5$ (left-hand window) and $h = 7$ (right-hand window). The scale is the same on all axes.

is a contour map of the density perturbation function $\bar{\rho}$, obtained from the same large run (with $M = N = 81$ Fourier coefficients) illustrated in Figure 7. The tightly coiled region at the rim of the plume cap, at a height of about $z = 4.7$, can be seen clearly in the figure. To obtain the diagram on the right, which shows the effective “interface”, the density contour at the value $\bar{\rho} = 0.04$ was extracted from the picture on the left, and rotated about the z -axis so as to illustrate the full axisymmetric geometry of the plume. For additional ease of viewing, a wedge has been cut out of the interfacial surface, by rotating the density contour only through the angles $-\pi/4 < \theta < 5\pi/4$ about the z -axis, so that the structure interior to the plume might become visible. The stem of the plume first widens a little, at about height $z = 2$, before narrowing a little at greater heights. Eventually, it rolls over to form the plume cap as shown, with an axisymmetric coiled region at the edge of the cap.

To conclude this presentation of results, we show in Figure 10 two different forced plumes at the same time $t = 10$, but with different channel heights $h = 5$ for the image on the left and $h = 7$ for the image on the right. Only the portion $0 < r < 3$, $0 < z < 5$ is shown in each case, so as to facilitate comparison of the two. These images were generated using $M = N = 51$ Fourier coefficients, which gives highly accurate results at this time $t = 10$. This figure confirms that the overturning of the plume that has happened in each case is not caused by the presence of the upper wall in this instance, since the two results are almost identical. Thus, it may be inferred that the

mushroom-shaped cap of the plume is a result of the vortex induced in the fluid by the motion of the lighter Fluid 1 itself, as studied in Figures 4, 5 and 8.

6. Discussion and conclusion

We have studied in detail the development of a plume in a fluid, extending the work of Russell et al. [29] from planar flow to the present cylindrical geometry. In axisymmetric outflow from a point source in a fluid in otherwise three-dimensional geometry, it was found recently by Forbes [12] that fluid ejection resulted in an essentially one-sided plume, without significant overturning; this is strongly at odds with the analogous two-dimensional flow from a line sink, in which outflow plumes of any mode number may arrange themselves around the line source, and each forms an overturning mushroom shape after sufficient time elapses [11]. The analogous question then naturally arises here, too. In two-dimensional geometry, Russell et al. [29] likewise found that rising plumes overturn to form mushroom-shaped structures and so the question is whether that also occurs in three-dimensional axisymmetric geometry or whether, instead, a jet forms without ever overturning, as for the problem considered in [12]. Unlike those cases of flow from isolated fluid sources, however, it has been established here that the three-dimensional flow situation is qualitatively similar to the two-dimensional outflow [29], and the axisymmetric plume also rises to form overturning structures. This is, of course, consistent with experience [36], and is evidently due to the influence of the bottom wall $z = 0$ on the flow and the strong rising vortex it helps to induce, surrounding the rising plume stem.

This paper has made a feature of the somewhat novel spectral method developed for this problem, in which a background flow is calculated, so as to satisfy the boundary conditions on the walls exactly. Then, in order also to satisfy the governing viscous equations of motion within the fluid, the spectral series representations are added to the background flow; the basis functions for these Fourier-type series must be chosen so as to vanish appropriately at the walls, since the wall boundary conditions are already accounted for by the background flow. Like any solution method, spectral approaches have some drawbacks, the most obvious being the evident need to choose basis functions carefully and then carry out significant amounts of algebra. However, there are also significant advantages in the present spectral approach. In many numerical solution techniques, solving the Poisson equation (2.13) for Ψ , given ζ , is an arduous task that must be carried out iteratively at each time step, but the advantage of the present semi-analytical approach is that this equation is solved immediately by the form (4.3) of the spectral representation. In addition, derivatives of quantities are carried out essentially exactly, and convergence of the representative series can be outstandingly good [7]. Here, this allowed the vorticity to be obtained so accurately that it was possible to observe in Figure 5 that the vorticity is essentially zero everywhere in the flow, except in the interfacial zone. This is closely analogous to the situation that occurs in unstable interfacial flows such as the Rayleigh–Taylor flow [10]. This suggests strongly that, in a plume model that postulated an infinitesimally thin interface, rather than the interfacial zone of finite

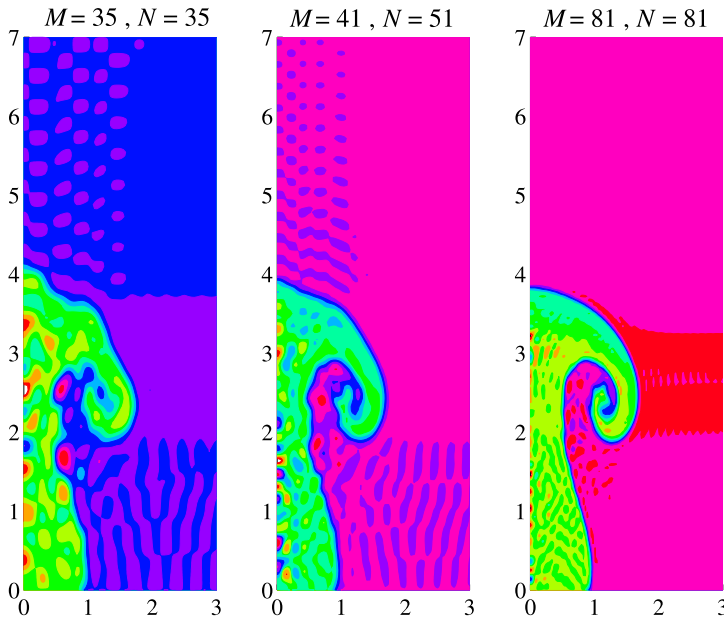


FIGURE 11. A comparison of numerical calculations of the same forced plume at time $t = 12$ for the case $h = 7$, $F = 2$ and $R_\infty = 5$. Results are presented for three different numbers of Fourier coefficients, as indicated. The scale is the same on all axes, but only the portion $0 < r < 3$ is shown. The coordinates r and z are plotted on the horizontal and vertical axes, respectively.

width used here, a singularity in the curvature of the interface would be likely to occur within finite time, as predicted first by Moore [25].

We have paid close attention to the convergence properties of the Fourier-series representations of the flow quantities and density perturbation function used throughout this work, and a brief analysis of the convergence behaviour is given in Figure 11. Here, the program was run using a 201×201 array of mesh points over the fluid domain, but for three different sets of numbers of Fourier coefficients. The left-most diagram was obtained from a run using $M = N = 35$ coefficients and gives only a coarse indication of the plume shape and location, although it is still sufficiently accurate to show that the plume has overturned. We have found that, while $M = N = 35$ coefficients yields good results for times in the approximate interval $0 < t < 10$, it is not really capable of following the solution at later times, because this number of coefficients is not sufficient to resolve the fine structure and small length scales associated with the plume roll up. Consequently, results at this time $t = 12$ would not normally be presented with $N = M = 35$. An additional feature of this graph is the presence of a mottled pattern over most of the fluid domain. These are small oscillations due to Gibbs' phenomenon [33], which occurs when the solution changes more rapidly than the Fourier series can resolve.

The central picture in Figure 11 has been obtained at the same time $t = 12$ with $M = 41$, $N = 51$ Fourier coefficients. Although there are minor flaws, the resolution

has now increased sufficiently to allow a reasonable depiction of the complicated rolled up region, and the shape and location of the plume at this time are now predicted accurately. Small-amplitude oscillations associated with Gibbs' phenomenon [33] are still present in the results, however, although the contouring routine used here does exaggerate their importance. Nevertheless, this is more an aesthetic concern than a scientific one. The final diagram, at the right-hand side of Figure 11, has been obtained from a run that used $M = N = 81$ Fourier coefficients, and is now well converged, with smooth narrow interfacial regions and greatly reduced oscillations associated with Gibbs' phenomenon.

By modifying the basis functions used here, it is possible to solve other, related, axisymmetric plume problems. In the case of a forced plume ($F > 0$) with $D < 1$, the injected Fluid 1 is now more dense than the ambient Fluid 2 and so falls downwards to create a fountain-type flow. We have computed some such solutions, but these are not discussed here in the interests of space, since a different spectral representation is required. In the present paper, we have also ignored the narrow boundary layers that would form close to the upper and lower walls of the channel, and this is an appropriate approximation for laminar flows with the moderate Reynolds numbers ($Re \sim 10^3$, $Re \sim 10^4$) adopted in this study. For slower viscous outflows in which these boundary layers are of greater importance, we have also experimented with background flows that satisfy the biharmonic equation for Ψ , rather than the simpler inviscid background flows used here in Section 3. Additionally, the basis functions in the spectral series are more complicated, since they must additionally satisfy no-slip conditions at these two walls. We have obtained preliminary results with this approach, which will be documented elsewhere.

It is also possible to extend the approach presented here to account for fully time-dependent three-dimensional plume geometry. Since this necessarily involves an extra spatial dimension, solution methods for such problems involve an order of magnitude extra computing power, although the underlying spectral method is not greatly more complicated than that developed here. Such computations would require a substantially more powerful machine than used here, and perhaps also a different programming environment, and it is significant that most investigations of fully three-dimensional flows of this sort are therefore limited to linearized analyses, such as the stability calculation for helical waves on a fluid jet, presented recently by Vadivukkarasan and Panchagnula [34]. We have, in fact, developed spectral approaches that can account for such three-dimensional time-dependent fluid geometry, and these will be discussed in a future article.

Acknowledgements

This work has been supported in part by Australian Research Council grant number DP140100094. We are grateful for critical comments from an anonymous referee, which have improved substantially the quality of the results presented in this paper.

References

- [1] M. Abramowitz and I. A. Stegun (eds), *Handbook of mathematical functions* (Dover, New York, 1972).
- [2] M. J. Andrews and S. B. Dalziel, “Small Atwood number Rayleigh–Taylor experiments”, *Philos. Trans. R. Soc. Lond. Ser. A* **368** (2010) 1663–1679; doi:10.1098/rsta.2010.0007.
- [3] K. E. Atkinson, *Elementary numerical analysis* (Wiley, New York, 1985).
- [4] G. Baker, R. E. Caffisch and M. Siegel, “Singularity formation during Rayleigh–Taylor instability”, *J. Fluid Mech.* **252** (1993) 51–78; doi:10.1017/S0022112093003660.
- [5] G. R. Baker and L. D. Pham, “A comparison of blob methods for vortex sheet roll-up”, *J. Fluid Mech.* **547** (2006) 297–316; doi:10.1017/S0022112005007305.
- [6] G. K. Batchelor, *An introduction to fluid dynamics* (Cambridge University Press, Cambridge, 1967).
- [7] J. P. Boyd, *Chebyshev and Fourier spectral methods*, 2nd edn (Dover, New York, 2001).
- [8] J. Craske and M. van Reeuwijk, “Generalised unsteady plume theory”, *J. Fluid Mech.* **792** (2016) 1013–1052; doi:10.1017/jfm.2016.72.
- [9] D. E. Farrow and G. C. Hocking, “A numerical model for withdrawal from a two-layer fluid”, *J. Fluid Mech.* **549** (2006) 141–157; doi:10.1017/S0022112005007561.
- [10] L. K. Forbes, “The Rayleigh–Taylor instability for inviscid and viscous fluids”, *J. Engrg. Math.* **65** (2009) 273–290; doi:10.1007/s10665-009-9288-9.
- [11] L. K. Forbes, “A cylindrical Rayleigh–Taylor instability: radial outflow from pipes or stars”, *J. Engrg. Math.* **70** (2011) 205–224; doi:10.1007/s10665-010-9374-z.
- [12] L. K. Forbes, “Rayleigh–Taylor instabilities in axi-symmetric outflow from a point source”, *ANZIAM J.* **53** (2011) 87–121; doi:10.1017/S1446181112000090.
- [13] L. K. Forbes, “How strain and spin may make a star bipolar”, *J. Fluid Mech.* **746** (2014) 332–367; doi:10.1017/jfm.2014.130.
- [14] L. Gómez, L. F. Rodríguez and L. Loinard, “A one-sided knot ejection at the core of the HH 111 outflow”, *Rev. Mex. Astron. Astrofís.* **49** (2013) 79–85; <http://www.scielo.org.mx/pdf/rmaa/v49n1/v49n1a9.pdf>.
- [15] I. S. Gradshteyn and I. M. Ryzhik, *Tables of integrals, series and products*, 6th edn (Academic Press, San Diego, CA, 2000).
- [16] G. C. Hocking and L. K. Forbes, “Steady flow of a buoyant plume into a constant-density layer”, *J. Engrg. Math.* **67** (2010) 341–350; doi:10.1007/s10665-009-9324-9.
- [17] D. E. Horsley, “Bessel phase functions: calculation and application”, *Numer. Math.* **136** (2017) 679–702; doi:10.1007/s00211-016-0853-7.
- [18] G. R. Hunt and H. C. Burridge, “Fountains in industry and nature”, *Annu. Rev. Fluid Mech.* **47** (2015) 195–220; doi:10.1146/annurev-fluid-010313-141311.
- [19] G. R. Hunt and N. B. Kaye, “Lazy plumes”, *J. Fluid Mech.* **533** (2005) 329–338; doi:10.1017/S002211200500457X.
- [20] R. Krasny, “Desingularization of periodic vortex sheet roll-up”, *J. Comput. Phys.* **65** (1986) 292–313; doi:10.1016/0021-9991(86)90210-X.
- [21] N. A. Letchford, L. K. Forbes and G. C. Hocking, “Inviscid and viscous models of axisymmetric fluid jets or plumes”, *ANZIAM J.* **53** (2012) 228–250; doi:10.1017/S1446181112000156.
- [22] R. V. E. Lovelace, M. M. Romanova, G. V. Ustyugova and A. V. Koldoba, “One-sided outflows/jets from rotating stars with complex magnetic fields”, *Mon. Not. R. Astron. Soc.* **408** (2010) 2083–2091; doi:10.1111/j.1365-2966.2010.17284.x.
- [23] C. Matsuoka and K. Nishihara, “Analytical and numerical study on a vortex sheet in incompressible Richtmyer–Meshkov instability in cylindrical geometry”, *Phys. Rev. E* **74** (2006); article 066303, 12 pages; doi:10.1103/PhysRevE.74.066303.
- [24] K. O. Mikaelian, “Rayleigh–Taylor and Richtmyer–Meshkov instabilities and mixing in stratified cylindrical shells”, *Phys. Fluids* **17** (2005); article 094105, 13 pages; doi:10.1063/1.2046712.
- [25] D. W. Moore, “The spontaneous appearance of a singularity in the shape of an evolving vortex sheet”, *Proc. R. Soc. Lond. Ser. A* **365** (1979) 105–119; doi:10.1098/rspa.1979.0009.

- [26] B. R. Morton, G. I. Taylor and J. S. Turner, “Turbulent gravitational convection from maintained and instantaneous sources”, *Proc. R. Soc. Lond. Ser. A* **234** (1956) 1–23; doi:10.1098/rspa.1956.0011.
- [27] G. Proskurowski, M. D. Lilley, D. S. Kelley and E. J. Olson, “Low temperature volatile production at the Lost City Hydrothermal Field, evidence from a hydrogen stable isotope geothermometer”, *Chem. Geol.* **229** (2006) 331–343; doi:10.1016/j.chemgeo.2005.11.005.
- [28] Lord Rayleigh, “Investigation of the character of the equilibrium of an incompressible heavy fluid of variable density”, *Proc. Lond. Math. Soc. (3)* **14** (1883) 170–177; doi:10.1112/plms/s1-14.1.170.
- [29] P. S. Russell, L. K. Forbes and G. C. Hocking, “The initiation of a planar fluid plume beneath a rigid lid”, *J. Engrg. Math.* **106** (2017) 107–121; doi:10.1007/s10665-016-9895-1.
- [30] D. H. Sharp, “An overview of Rayleigh–Taylor instability”, *Physica D* **12** (1984) 3–18; doi:10.1016/0167-2789(84)90510-4.
- [31] S. W. Stahler and F. Palla, *The formation of stars* (Wiley-VCH, Berlin, 2004).
- [32] Sir G. I. Taylor, “The instability of liquid surfaces when accelerated in a direction perpendicular to their planes, I”, *Proc. R. Soc. Lond. Ser. A* **201** (1950) 192–196; doi:10.1098/rspa.1950.0052.
- [33] L. N. Trefethen, “Finite difference and spectral methods for ordinary and partial differential equations”, unpublished text, 1996; <http://people.maths.ox.ac.uk/trefethen/pdtext.html>.
- [34] M. Vadivukkarasan and M. V. Panchagnula, “Combined Rayleigh–Taylor and Kelvin–Helmholtz instabilities on an annular liquid sheet”, *J. Fluid Mech.* **812** (2017) 152–177; doi:10.1017/jfm.2016.784.
- [35] G. von Winckel, *lgwt.m*, at: MATLAB file exchange website (2004); <http://www.mathworks.com/matlabcentral/fileexchange/loadFile.do?objectId=4540&objectType=file>.
- [36] A. W. Woods, “Turbulent plumes in nature”, *Annu. Rev. Fluid Mech.* **42** (2010) 391–412; doi:10.1146/annurev-fluid-121108-145430.